SUPPORTING INFORMATION

Rational Design of Low-Dimensional Hybrid Organic/Inorganic Interfaces with Enhanced Second-Harmonic Generation

Michele Guerrini[1], M. Sufyan Ramzan[1], and Caterina Cocchi[1,2]

[1]Friedrich-Schiller-Universität Jena, Institut für Festkörpertheorie und -optik, 07743 Jena, Germany
[2]Friedrich-Schiller-Universität Jena, Abbe Center of Photonics, 07745 Jena, Germany

Contents

S1 Reconstruction of the Molecular Hyperpolarizability Tensors **S2**
S1.1 Orr–Ward sum-over-states formulation and gauge invariance S2
S1.2 First-Principles Tensor Construction from Linear-Response TDDFT S2

S2 Computational Details **S3**
S2.1 Ground-state and TDDFT calculations S3
S2.2 LayerPCM substrate screening S6
S2.3 Substrate Sensitivity and Robustness Analysis S7

S3 Extended Optical Response and Spectral Comparisons **S8**
S3.1 Additional SHG polar patterns S8
S3.2 Comparative Analysis with Pristine Perylene Signatures S15

S4 First-Principles Analysis of Selected Hybrid Organic/Inorganic Interfaces **S19**

S1 Reconstruction of the Molecular Hyperpolarizability Tensors

S1.1 Orr–Ward sum-over-states formulation and gauge invariance

To evaluate the frequency-dependent molecular hyperpolarisability tensor, we employ the Orr–Ward sum-over-states (SOS) perturbative expression [1]:

$$\beta_{ijk}(-2\omega;\omega,\omega) = \frac{1}{\hbar^2}\sum_{n,m\neq g}\frac{\mu^i_{gn}\,\bar{\mu}^j_{nm}\,\mu^k_{mg}}{(\omega_{ng}-2\omega-i\Gamma)(\omega_{mg}-\omega-i\Gamma)}, \tag{1}$$

where $\mu^i_{gn} = \langle g|\hat{\mu}_i|e_n\rangle$ represents the ground-to-excited state transition dipole moments, $\hbar\Omega_n$ denotes vertical excitation energies, and Γ is the phenomenological homogeneous linewidth. The factor $\bar{\mu}^j_{nm} = \langle e_n|\hat{\mu}_j|e_m\rangle - \delta_{nm}\langle g|\hat{\mu}_j|g\rangle$ incorporates the fluctuation matrix elements of the dipole operator: yielding:

$$\bar{\mu}^j_{nm} = \langle e_n|\hat{\mu}_j|e_m\rangle - \delta_{nm}\langle g|\hat{\mu}_j|g\rangle. \tag{2}$$

By subtracting the ground-state dipole expectation value $\langle g|\hat{\mu}_j|g\rangle$, this formulation enforces strict gauge and origin invariance under a uniform coordinate shift of the electrostatic reference ($\hat{\mu}_j \to \hat{\mu}_j + c_j\mathbb{1}$). While such a shift alters absolute expectation values, its contribution cancels identically in Eq. (1):

$$\langle e_n|\hat{\mu}_j + c_j|e_m\rangle - \delta_{nm}\langle g|\hat{\mu}_j + c_j|g\rangle = \bar{\mu}^j_{nm}. \tag{3}$$

For diagonal intermediate states ($n = m$), this fluctuation term converts the excited-state expectation value into the net charge-redistribution vector upon vertical excitation, $\Delta\mu^j_n = \langle e_n|\hat{\mu}_j|e_n\rangle - \langle g|\hat{\mu}_j|g\rangle$. For off-diagonal transitions ($n \neq m$), the subtraction term vanishes, recovering the standard excited-to-excited transition dipole moments. Furthermore, because energy denominators depend solely on excitation differences ($\hbar\Omega_n = E_n - E_g$), the expression remains rigorous under uniform energy shifts. For centrosymmetric geometries, this fluctuation form guarantees the exact cancellation of all inversion-forbidden contributions, recovering the exact condition $\boldsymbol{\beta}^{\mathrm{mol}} \equiv \mathbf{0}$ required by Neumann's principle.

To isolate the spatial orientation dependence from electronic structure perturbations, the intrinsic molecular spectral parameters entering Eq. (1) are evaluated once in the unperturbed reference frame ($\theta = 0°$). The screening framework operates in the quasi-static limit ($\hbar\omega \to 0$, with a constant broadening $\Gamma = 0.05$ eV), reducing the Orr–Ward denominators to energy products ($\hbar\Omega_n \cdot \hbar\Omega_m$). During spatial orientation scans, the underlying electronic spectrum (excitation energies $\hbar\Omega_n$, transition dipoles $\boldsymbol{\mu}_{gn}$, and fluctuation matrices $\bar{\boldsymbol{\mu}}_{nm}$) remains fixed, while the rank-3 hyperpolarizability tensor $\boldsymbol{\beta}^{\mathrm{mol}}$ and the ground-state dipole vector $\boldsymbol{\mu}_{gg}$ are rigidly rotated into the laboratory framework. This cleanly isolates spatial tensor contraction pathways and electric-field-induced SHG (EFISH) phase interactions from orientation-dependent electronic hybridization.

S1.2 First-Principles Tensor Construction from Linear-Response TDDFT

The transition dipoles and excited-state matrix elements are analytically reconstructed from Casida's linear-response TDDFT framework [2]. First, the ground-to-excited transition dipole moments are mapped from the normalized eigenvectors $F^{(I)}_{ia}$ of the symmetrized Casida matrix:

$$\mu^{\alpha}_{gI} = \sum_{ia} F^{(I)}_{ia}\sqrt{\frac{2\varepsilon_{ia}}{\Omega_I}}\,d^{\alpha}_{ia}, \tag{4}$$

where $\varepsilon_{ia} = \varepsilon_a - \varepsilon_i$ is the single-particle Kohn-Sham gap, Ω_I is the excitation energy, and d^{α}_{ia} represents the signed Cartesian KS dipole matrix elements derived directly from the underlying spatial

multipole distribution. Evaluating the full signed orientation of d_{ia}^{α} is mandatory; utilizing absolute values introduces artificial symmetry-breaking terms that yield spurious, non-zero β elements for centrosymmetric systems.

To map the off-diagonal excited-to-excited dipole matrix transitions ($\bar{\mu}_{nm}^{j}$), we apply the Slater-Condon rules on single-particle determinants. This isolates the distinct virtual–virtual (VV) and occupied–occupied (OO) orbital contribution pathways:

$$\bar{\mu}_{nm}^{j} = \underbrace{\sum_{i,a,b} C_{ia}^{(n)} C_{ib}^{(m)}\, \mu_{ab}^{(v)}}_{\text{virtual–virtual (VV)}} - \underbrace{\sum_{i,j',a} C_{ia}^{(n)} C_{j'a}^{(m)}\, \mu_{ij'}^{(o)}}_{\text{occupied–occupied (OO)}}\,, \tag{5}$$

where $C_{ia}^{(I)} = F_{ia}^{(I)} \sqrt{2\varepsilon_{ia}/\Omega_I}$ represents the corrected excitation amplitudes related to the traditional transition vectors $(X+Y)$, while $\mu_{ab}^{(\mathrm{v})}$ and $\mu_{ij'}^{(\mathrm{o})}$ are the virtual-space and occupied-space tensors, respectively. The resulting contraction matrix is assembled via $W_{nm}^{(j)} = \bar{\mu}_{nm}^{j}/D_{nm}$, with

$$D_{nm} = (\Omega_n - 2\hbar\omega - i\Gamma)\,(\Omega_m - \hbar\omega - i\Gamma)\,, \tag{6}$$

yielding the complete hyperpolarizability tensor components $\beta_{ijk} = \sum_{n,m} \mu_{gn}^{i} W_{nm}^{(j)} \mu_{mg}^{k}$. The numerical stability and accuracy of this reconstruction were validated using a centrosymmetric magnesium phthalocyanine as a test system (D_{4h} symmetry, 100 explicit excited states), yielding a residual numerical noise baseline of $\|\beta\|_F = 5.2 \times 10^{-2}\,(e\text{Å})^3/\text{eV}^2$ against an exact analytical limit of zero.

To quantify the microscopic contribution of individual excited states to the second-order optical response, we construct a state-resolved decomposition of the sum-over-states (SOS) hyperpolarizability tensor. For any pair of intermediate excited states (I, J) within the active manifold, the third-rank transition tensor element is evaluated via the standard perturbation expansion:

$$T_{IJ,ijk} = \frac{\mu_{gI}^{i}\, \bar{\mu}_{IJ}^{j}\, \mu_{Jg}^{k}}{D_{IJ}}, \tag{7}$$

To assess the isotropic weight of each state pair without polarization bias, we define the symmetrized pair tensor $T_{IJ}^{\mathrm{sym}} = T_{II}$ for $I = J$ and $T_{IJ}^{\mathrm{sym}} = T_{IJ} + T_{JI}$ for $I \neq J$. The relative fractional contribution a_{IJ} of state pair (I, J) to the global hyperpolarizability tensor topology is computed using the Frobenius norm over Cartesian components:

$$a_{IJ} = 100 \times \frac{\|T_{IJ}^{\mathrm{sym}}\|_F}{\sum_{K \leq L} \|T_{KL}^{\mathrm{sym}}\|_F}. \tag{8}$$

The net weight a_I of a specific electronic state I within the global SOS expansion is subsequently recovered by partitioning off-diagonal cross-contributions symmetrically across participating state channels:

$$a_I = a_{II} + \frac{1}{2} \sum_{J \neq I} a_{\min(I,J),\max(I,J)}, \tag{9}$$

ensuring normalization over the active SOS space ($\sum_I a_I = 100\%$).

S2 Computational Details

S2.1 Ground-state and TDDFT calculations

Ground-state DFT and linear-response TDDFT calculations for the zero-tilt seed geometries of pristine perylene, SA-F_4-, LA-F_4-, SA-F_6-, and LA-F_6-perylene were performed with the `Octopus`

code [3] using HGH-LDA pseudopotentials [4], and the Perdew–Zunger LDA functional [5]. The real-space simulation region was a finite spherical box of radius 6.0 Å with grid spacing 0.24 Å. Singlet excited states were computed in the Casida formulation of TDDFT [2]. Each calculation included 100 extra states spanning a 30 eV KS transition-energy window. To construct the excited-state manifold entering the SOS expansion, the first 100 Casida excitations were printed for each molecule. To balance numerical precision with computational efficiency, states were truncated using an oscillator strength threshold of $f_I \geq 10^{-3}$, discarding dark states with negligible transition dipole moments that do not contribute to the second-order susceptibility. If no states passed this threshold, the parser defaulted to all printed states. Table S1 summarizes the evaluated excitation energy windows and the state counts retained for the SOS reconstruction.

Table S1: Summary of Casida calculations for the zero-tilt reference molecules, detailing the evaluated singlet state range, the subset of optically active transitions satisfying the oscillator strength criterion ($f_I \geq 10^{-3}$), the spanned excitation energy window, and the fundamental optical gap (E_1)..

System	Printed states	Retained states	E_I window (eV)	Lowest bright (eV)
perylene	1–100	44	2.55–6.89	2.55
SA-F_4	1–100	62	2.64–6.96	2.64
LA-F_4	1–100	54	2.18–6.47	2.18
SA-F_6	1–100	52	2.31–6.59	2.31
LA-F_6	1–100	54	2.23–6.69	2.23

The resulting absorption spectra (Figure S1) map the excited-state transition density and validate the energetic placement of bright channels relative to the fundamental gap. Note that these spectra serve descriptor and validation purposes; they are not used as finite-frequency laser SHG spectra, as all orientation tilt trends are evaluated within the quasi-static descriptor framework ($\hbar\omega \to 0$).

Table S2 lists the energy, oscillator strength, orbital composition, and state-resolved contribution a_I for the ten dominant excited states per system.

Table S2: Casida excited-state descriptors for the ten dominant excited states used to build the molecular hyperpolarizability tensor from the Orr–Ward SOS: excitation energy E_I, oscillator strength f_I, orbital composition (only transitions with at least 10% weight are reported), and the state-resolved SOS contribution a_I.

System	State	E_I (eV)	f_I	KS composition	a_I (%)
perylene	S1	2.552	0.283	H→L (95%)	5.5
perylene	S15	4.762	0.037	H-1→L+1 (65%), H-3→L+4 (12%)	3.8
perylene	S23	5.096	0.007	H-3→L+2 (42%), H-4→L+2 (25%), H-2→L+4 (17%)	3.5
perylene	S30	5.498	0.698	H-2→L+2 (64%), H-8→L (11%)	6.9
perylene	S37	5.821	0.245	H→L+18 (46%), H→L+16 (17%)	5.0
perylene	S43	5.973	0.353	H→L+17 (88%)	10.1
perylene	S58	6.285	0.520	H→L+21 (66%)	8.5
perylene	S59	6.289	1.044	H→L+21 (33%), H-1→L+3 (17%), H→L+18 (15%)	11.5
perylene	S69	6.448	0.010	H→L+22 (43%), H-7→L+1 (16%), H-14→L (12%)	4.1

Continued on next page

Table S2: Casida excited-state descriptors, continued.

System	State	E_I (eV)	f_I	KS composition	a_I (%)
perylene	S72	6.473	0.644	H-3→L+4 (15%)	7.5
SA-F_4	S1	2.637	0.235	H→L (93%)	9.7
SA-F_4	S3	3.302	0.026	H→L+1 (91%)	3.7
SA-F_4	S4	3.353	0.039	H-2→L (80%), H→L+4 (14%)	3.9
SA-F_4	S31	5.445	0.528	H-4→L+1 (53%), H-3→L+3 (33%)	5.0
SA-F_4	S39	5.677	0.335	H-3→L+4 (30%), H→L+15 (22%)	4.9
SA-F_4	S43	5.778	0.252	H-3→L+3 (21%), H-3→L+4 (17%), H-5→L+1 (14%)	4.4
SA-F_4	S44	5.795	0.217	H-4→L+4 (25%), H→L+18 (12%), H-1→L+10 (10%), H-6→L (10%)	3.5
SA-F_4	S45	5.848	0.281	H-4→L+4 (30%), H→L+18 (24%), H-8→L (13%)	4.4
SA-F_4	S57	6.104	0.548	H-1→L+10 (23%), H-5→L+3 (16%), H→L+18 (15%)	7.2
SA-F_4	S90	6.741	0.434	H-5→L+4 (38%), H-8→L+2 (17%), H-5→L+3 (14%)	3.7
LA-F_4	S1	2.178	0.225	H→L (93%)	20.6
LA-F_4	S5	3.109	0.020	H-2→L (67%), H→L+6 (30%)	5.5
LA-F_4	S11	3.827	0.067	H-1→L+1 (81%)	3.9
LA-F_4	S14	4.043	0.131	H-2→L+1 (42%), H-4→L (23%)	4.3
LA-F_4	S26	4.547	0.123	H-1→L+3 (36%), H-1→L+5 (28%), H-4→L+1 (13%)	4.7
LA-F_4	S28	4.689	0.047	H-3→L+1 (18%), H-2→L+6 (16%), H-4→L+1 (14%), H-6→L (14%), H-3→L+5 (12%)	3.2
LA-F_4	S38	5.080	0.233	H-3→L+3 (62%)	4.9
LA-F_4	S43	5.278	0.116	H-4→L+3 (57%), H-5→L+1 (11%)	3.2
LA-F_4	S49	5.473	0.273	H-5→L+1 (31%), H-3→L+5 (25%)	3.2
LA-F_4	S65	5.914	0.340	H-6→L+1 (24%), H-6→L+3 (18%), H-4→L+6 (11%)	2.9
SA-F_6	S1	2.313	0.198	H→L (91%)	16.3
SA-F_6	S6	3.287	0.024	H-2→L (43%), H→L+4 (30%), H-1→L (10%)	3.5
SA-F_6	S7	3.389	0.084	H-3→L (33%), H→L+4 (28%), H-2→L (18%)	7.3
SA-F_6	S14	3.927	0.090	H-4→L (41%), H→L+6 (28%)	5.1
SA-F_6	S33	4.872	0.104	H-1→L+5 (43%), H-3→L+4 (16%), H-2→L+5 (11%)	3.8
SA-F_6	S37	5.063	0.098	H-2→L+5 (31%), H-4→L+4 (13%), H-1→L+5 (10%)	3.8
SA-F_6	S39	5.111	0.372	H-3→L+4 (54%)	6.6
SA-F_6	S48	5.455	0.213	H→L+16 (53%), H-4→L+6 (14%), H-5→L+3 (13%)	3.8
SA-F_6	S67	5.949	0.686	H-5→L+4 (37%), H-9→L (14%), H-4→L+6 (12%), H-5→L+3 (11%)	4.3
SA-F_6	S72	6.087	0.189	H-6→L+4 (48%), H-5→L+6 (13%)	3.6
LA-F_6	S1	2.230	0.191	H→L (91%)	20.3
LA-F_6	S5	3.239	0.061	H-2→L (55%), H→L+4 (37%)	5.9
LA-F_6	S7	3.634	0.053	H→L+4 (49%), H-2→L (33%)	3.1
LA-F_6	S12	4.081	0.080	H-1→L+2 (69%), H-1→L+3 (10%)	3.3
LA-F_6	S22	4.703	0.170	H-1→L+4 (22%), H-3→L+4 (20%), H-6→L (14%), H→L+10 (11%), H-2→L+1 (11%)	3.7
LA-F_6	S23	4.723	0.124	H-3→L+1 (38%), H-3→L+2 (12%), H-4→L+3 (11%)	4.0
LA-F_6	S32	5.202	0.218	H-4→L+2 (32%), H-3→L+2 (20%), H-5→L (14%)	4.0
LA-F_6	S33	5.206	0.320	H-3→L+4 (22%), H→L+10 (16%), H-1→L+4 (13%)	3.9
LA-F_6	S38	5.328	0.395	H-3→L+3 (27%), H-4→L+3 (20%)	5.5
LA-F_6	S43	5.541	0.161	H→L+13 (54%), H-7→L (14%), H-1→L+10 (10%)	2.9

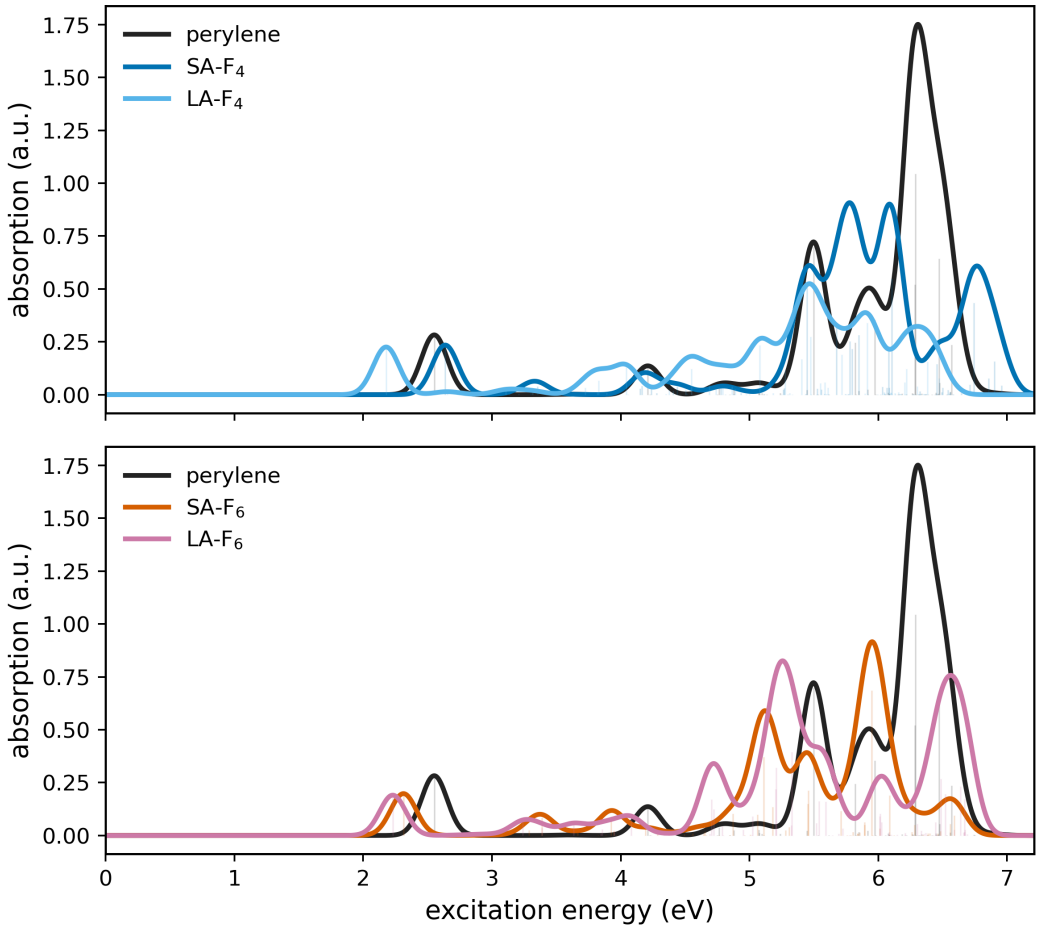

Figure S1: Calculated Casida absorption spectra for the zero-tilt reference systems embedded in a LayerPCM dielectric environment. (Top) Pristine perylene compared against the regoisomeric F_4 series (SA-F_4 and LA-F_4). (Bottom) Pristine perylene compared against the F_6 series (SA-F_6 and LA-F_6). Vertical bar spectra denote discrete TDDFT excitation energies and oscillator strengths (f_I); solid curves depict broadened spectral envelopes ($\sigma = 0.10$ eV).

S2.2 LayerPCM substrate screening

The substrate dielectric environment is modeled using `LayerPCM` [6], which maps the substrate layer stack onto frequency-dependent in-plane and out-of-plane dielectric constants. For the MoS_2 monolayer substrate, the adopted parameters are:

$$\varepsilon_{\parallel} = 16.52, \qquad \varepsilon_{\perp} = 10.08, \qquad d = 5.46\,\text{Å (monolayer effective depth)},$$

derived from bulk MoS_2 dielectric constants projected onto the monolayer geometry [6].

Substrate susceptibilities $\chi^{(2)}_{\text{sub}}$ and $\chi^{(3)}_{\text{sub}}$ are defined using normalized phenomenological values. Setting the leading in-plane amplitude $\chi^{(2)}_{yyy} = 1$ in the D_{3h}/C_{3v} convention sets the SHG intensity scale, with symmetry-related components matching signs (e.g. $\chi^{(2)}_{yxx} = \chi^{(2)}_{xxy} = \chi^{(2)}_{xyx} = -\chi^{(2)}_{yyy}$). All reported SHG intensities reflect coherent squared amplitudes relative to the choice of this substrate. The D_{3h} monolayer contains only in-plane $\chi^{(2)}$ components, whereas the C_{3v} Janus layer includes

additional out-of-plane elements $\chi^{(2)}_{zzz} = 0.25$ and $\chi^{(2)}_{zxx} = \chi^{(2)}_{xxz} = 0.15$. The D_{3d} bilayer consists of two D_{3h} layers in the inversion-symmetric 2H registry, causing the cancellation of the electric-dipole contribution. All three substrates share a unified normalized uniaxial $\chi^{(3)}$ tensor ($\chi^{(3)}_{xxxx} = \chi^{(3)}_{zzzz} = 1$ and $\chi^{(3)}_{xxyy} = \chi^{(3)}_{xxzz} = \chi^{(3)}_{zzxx} = 0.3$), with D_{3d} value obtained by coherently summing both monolayer contributions. These parameters act as off-resonant model parameters far from substrate excitonic resonances [7].

S2.3 Substrate Sensitivity and Robustness Analysis

To evaluate model sensitivity, substrate tensor components are scaled by a common multiplicative factor s applied across all non-zero $\chi^{(2)}_{\text{sub}}$ and $\chi^{(3)}_{\text{sub}}$ elements, preserving symmetry-imposed tensor ratios while varying the background strength. Figure S2 illustrates the maximum azimuthal SHG intensity across tilt angles for scale factors ranging from the molecule-only limit ($s = 0.001$) to an enhanced substrate limit ($s = 2.0$), centered on the reference model ($s = 1.0$).

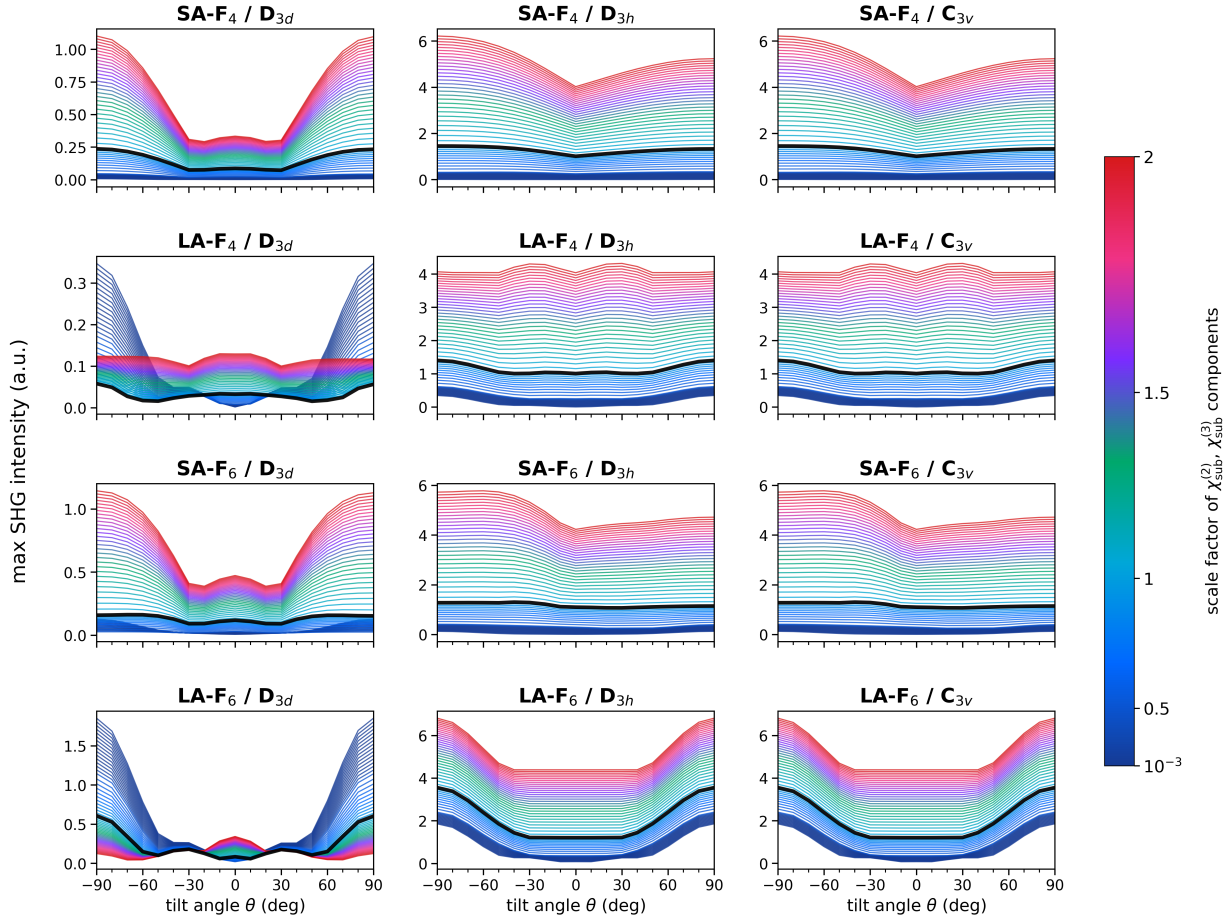

Figure S2: Robustness of the channel-maximised SHG tilt trends with respect to a common substrate tensor scaling factor s. Coloured curves span $s = 0.001$–2, while the black curve marks the reference model ($s = 1$). The $s = 0.001$ limit approximates the molecule-only response, whereas larger s values increase the substrate $\chi^{(2)}$ background and the $\chi^{(3)}$-mediated EFISH coupling without changing the relative ratios between symmetry-allowed substrate tensor components.

In the low-scale limit ($s \to 0$), all substrate classes collapse onto the molecule-only response ($\boldsymbol{\chi}^{(2)}_{\mathrm{mol}}$). The variation with tilt angle in this limit reflects changing projections of the anisotropic molecular tensor onto laboratory p, s, and z polarization channels. Increasing s enhances the substrate background and interference effects: for D_{3d}, it amplifies the $\boldsymbol{\chi}^{(3)}$-mediated EFISH coupling; for D_{3h} and C_{3v}, it scales coherent interference between molecular emission and the intrinsic substrate $\chi^{(2)}$. Although absolute signal strengths and near-degenerate isomer rankings shift with s, core conclusions remain invariant: high-tilt configurations enhance response, tilt-sign asymmetry stems from coherent substrate–molecule interference, and permanent dipole magnitudes alone are insufficient to predict SHG rankings.

S3 Extended Optical Response and Spectral Comparisons

S3.1 Additional SHG polar patterns

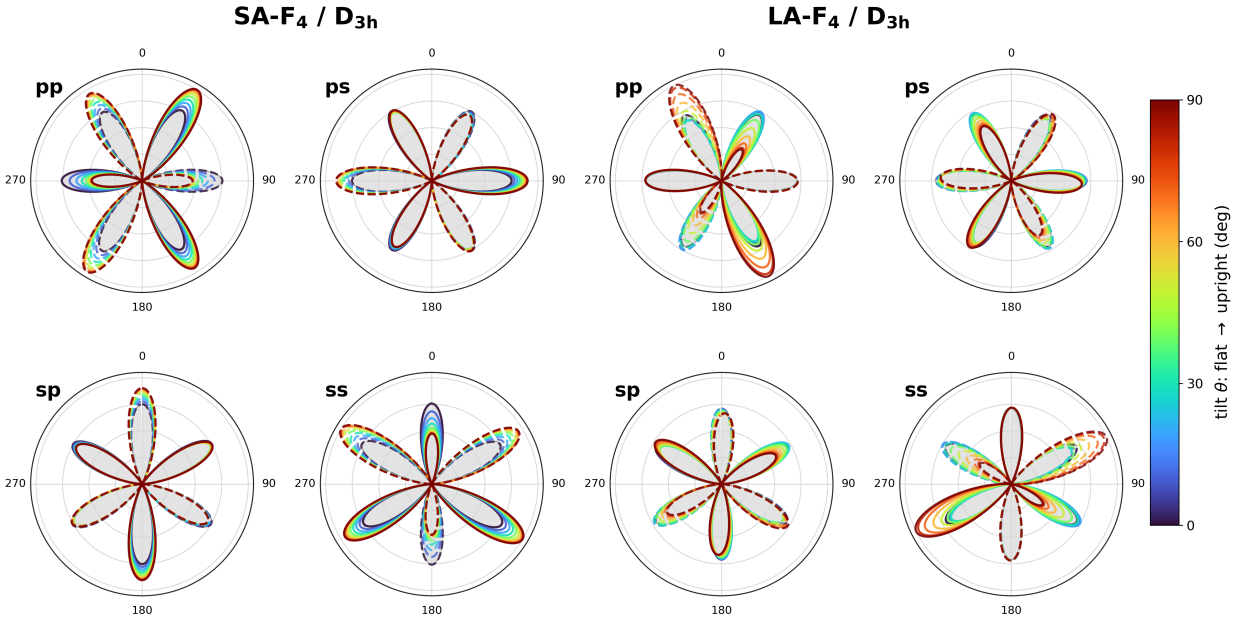

Figure S3: In-plane SHG polar patterns (*pp*, *ps*, *sp*, *ss*) on the D_{3h} monolayer for F_4-perylene **LA** (left, tilt about Y) and **SA** (right, tilt about X). The six-fold D_{3h} template is present at all tilt angles; the molecule breaks lobe equivalence, with constructive interference appearing as lobe growth (solid curves) and destructive interference as lobe shrinkage or sign reversal (dashed curves) depending on tilt sign. The gray filled lobes are the SHG polar plots of the isolated substrate

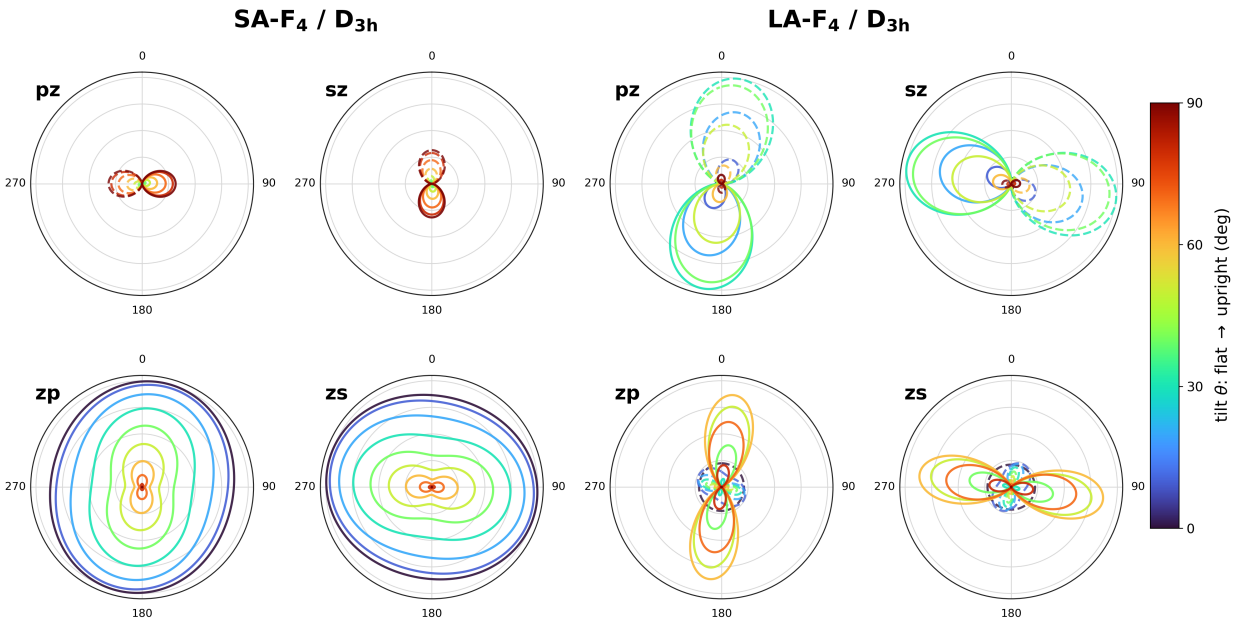

Figure S4: Mixed-z polar patterns (pz, sz, zp, zs) on the D_{3h} monolayer for F_4-perylene **LA** (left, tilt about Y) and **SA** (right, tilt about X) push-pull isomer configurations. The D_{3h} horizontal mirror forbids intrinsic z-odd components; all mixed-z response shown here is purely molecule-induced. The SA zp/zs patterns remain nearly circular, indicating $\chi_{zxx} \approx \chi_{zyy}$ and an almost isotropic projection of the in-plane nonlinear response onto the out-of-plane polarization channel.

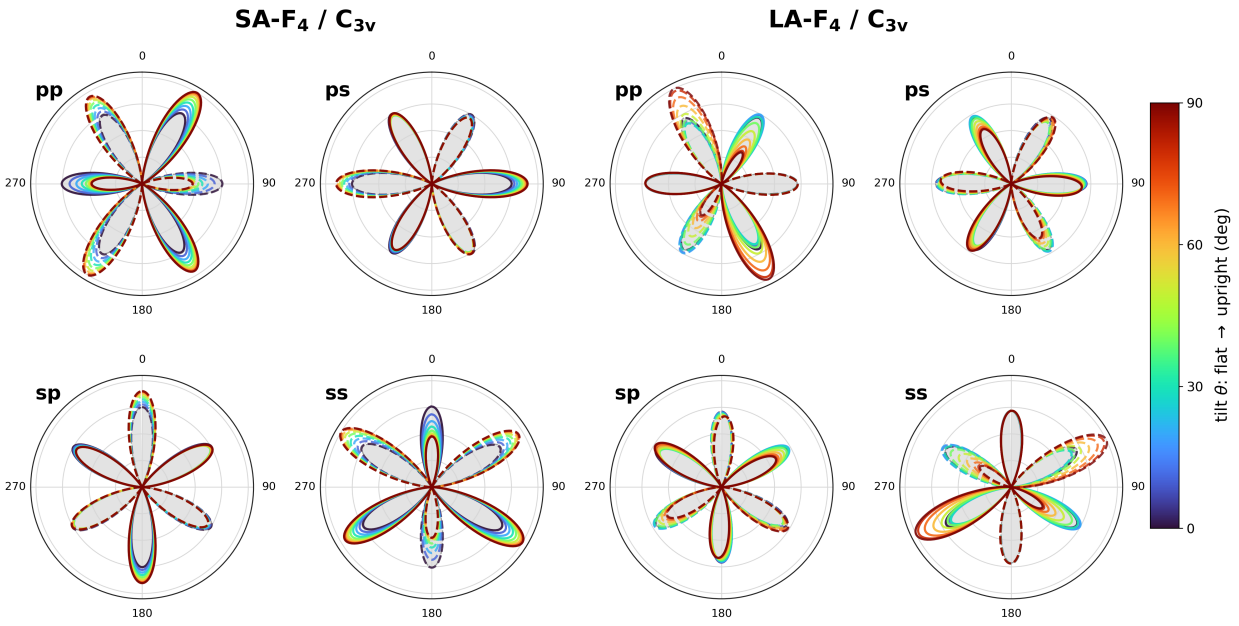

Figure S5: In-plane polar patterns on the non-centrosymmetric C_{3v} Janus-type layer for F_4-perylene **LA** (left, tilt about Y) and **SA** (right, tilt about X) push-pull isomer configurations. The in-plane pattern is nearly identical to the D_{3h} monolayer (both substrates share the same in-plane $\chi^{(2)}{}_{\mathrm{sub}}$ family), confirming that in-plane SHG is governed primarily by the shared trigonal symmetry. The gray filled lobes are the SHG polar plots of the isolated substrate

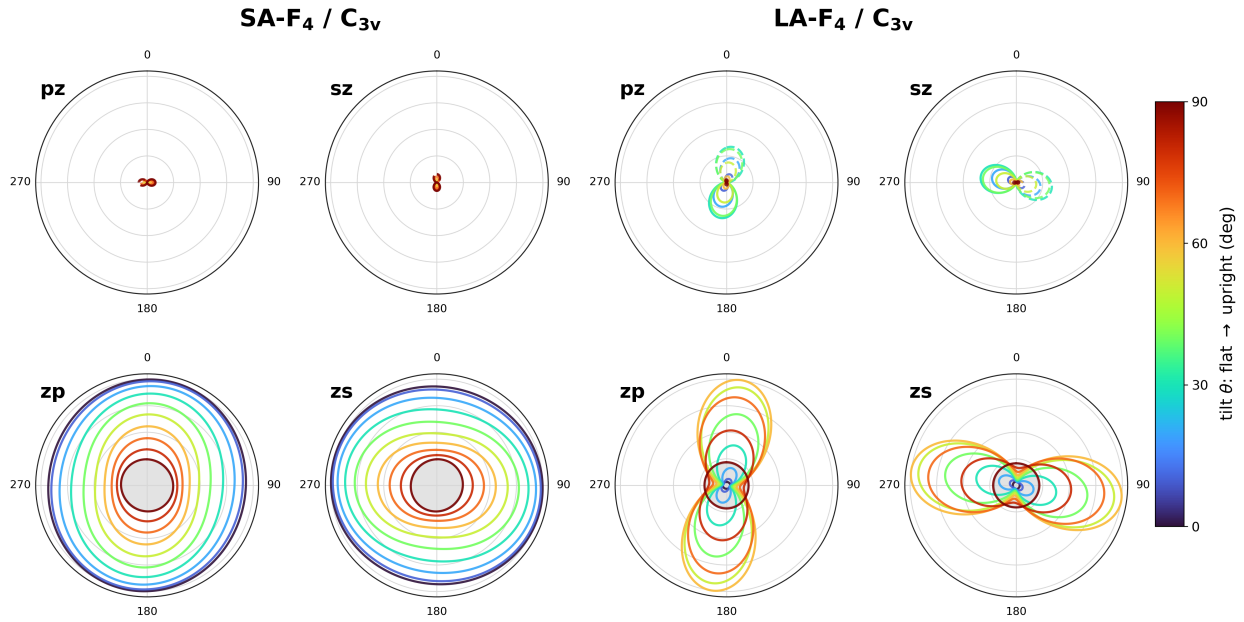

Figure S6: Mixed-z patterns on the C_{3v} Janus layer for F_4-perylene **LA** (left, tilt about Y) and **SA** (right, tilt about X) push-pull isomer configurations. C_{3v} permits intrinsic out-of-plane components ($\chi^{(2)}_{zzz}, \chi^{(2)}_{zxx}, \chi^{(2)}_{xxz}$), raising the zp/zs baseline relative to the D_{3h} case. The gray filled lobes are the SHG polar plots of the isolated substrate. The SA zp/zs polar patterns are nearly circular (isotropic), dominated by the substrate out-of-plane background at hight tilt angles where the in-plane component of the molecular dipole approaches zero.

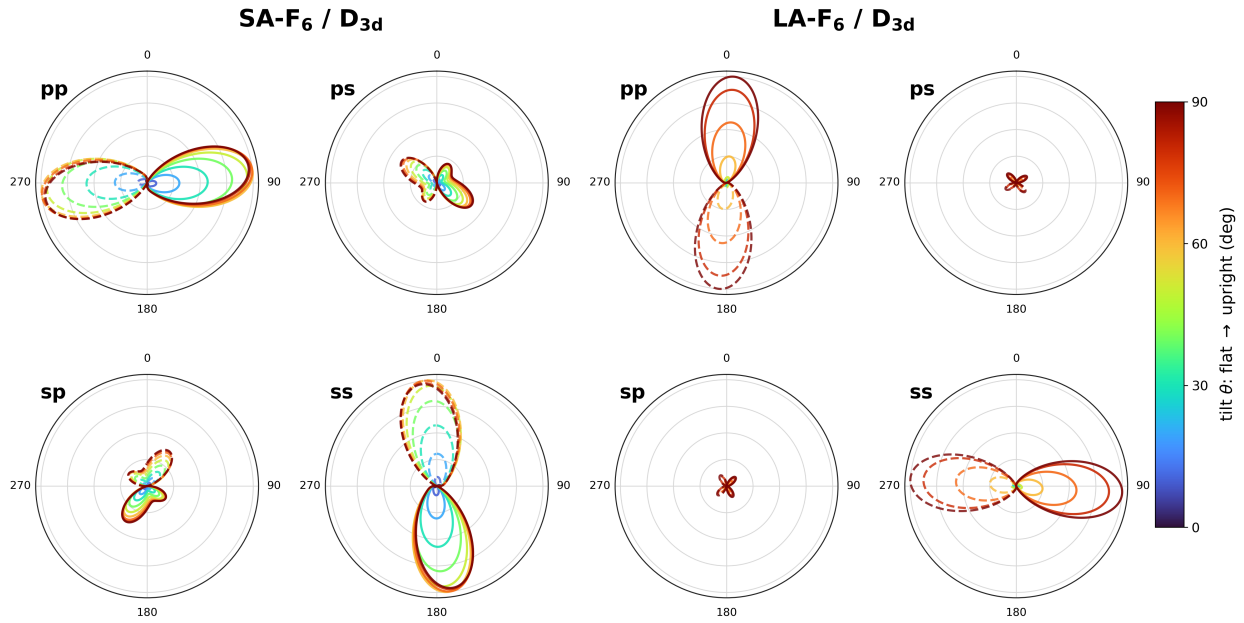

Figure S7: In-plane SHG polar plots of F_6-SA (left) and F_6-LA (right) push-pull isomer configurations on the D_{3d} centrosymmetric bilayer-type substrate.

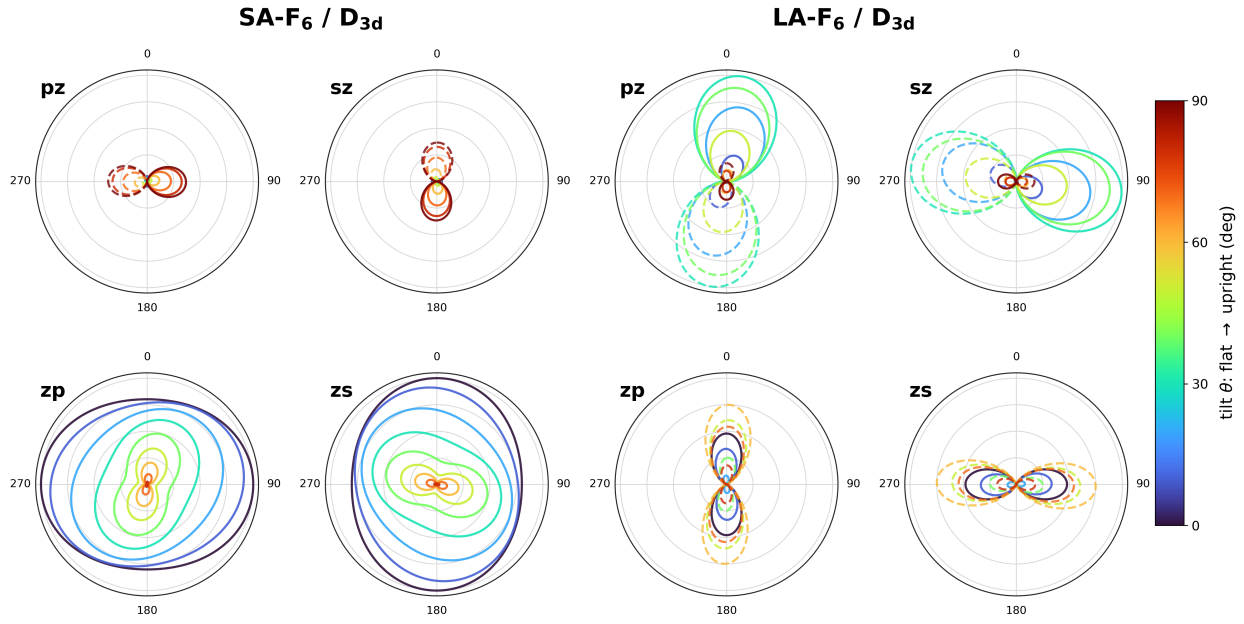

Figure S8: Mixed-z SHG polar plots of F_6-SA (left) and F_6-LA (right) push-pull isomer configurations on the centrosymmetric D_{3d} bilayer.

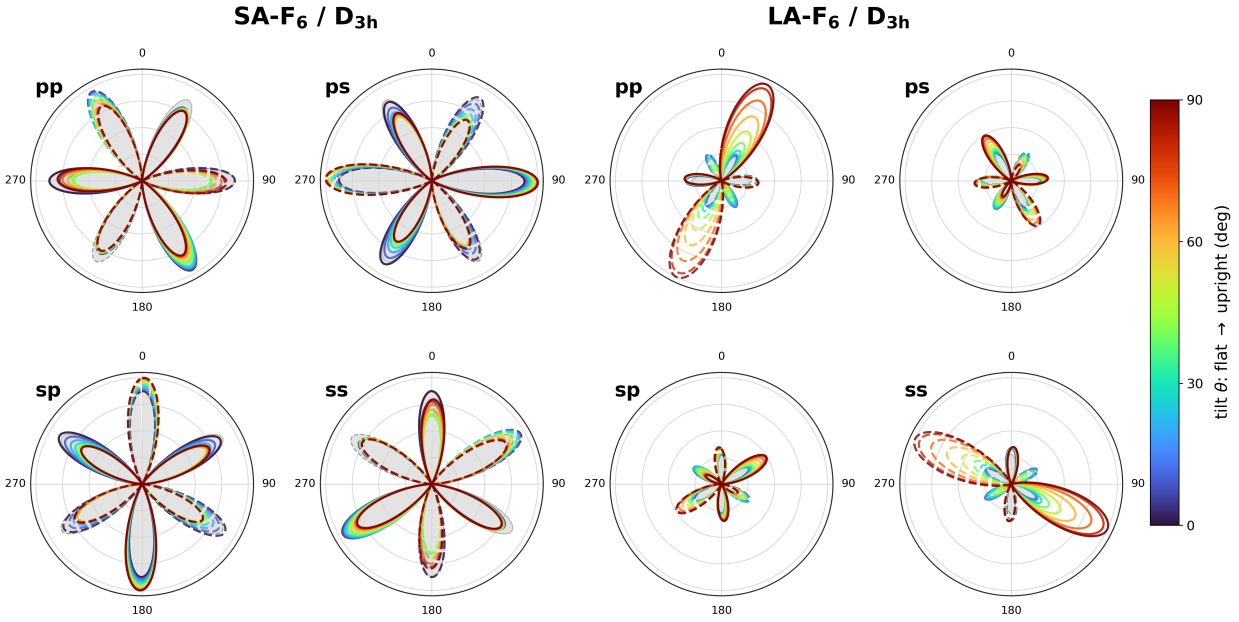

Figure S9: F_6-SA and F_6-LA in-plane polar pattern channels on the non-centrosymmetric D_{3h} monolayer-type substrate. The strong in-plane response at high tilt is consistent with the channel-resolved maximum SHG as function of the tilt angle shown in the corresponding main-text channel-resolved tilt curves.

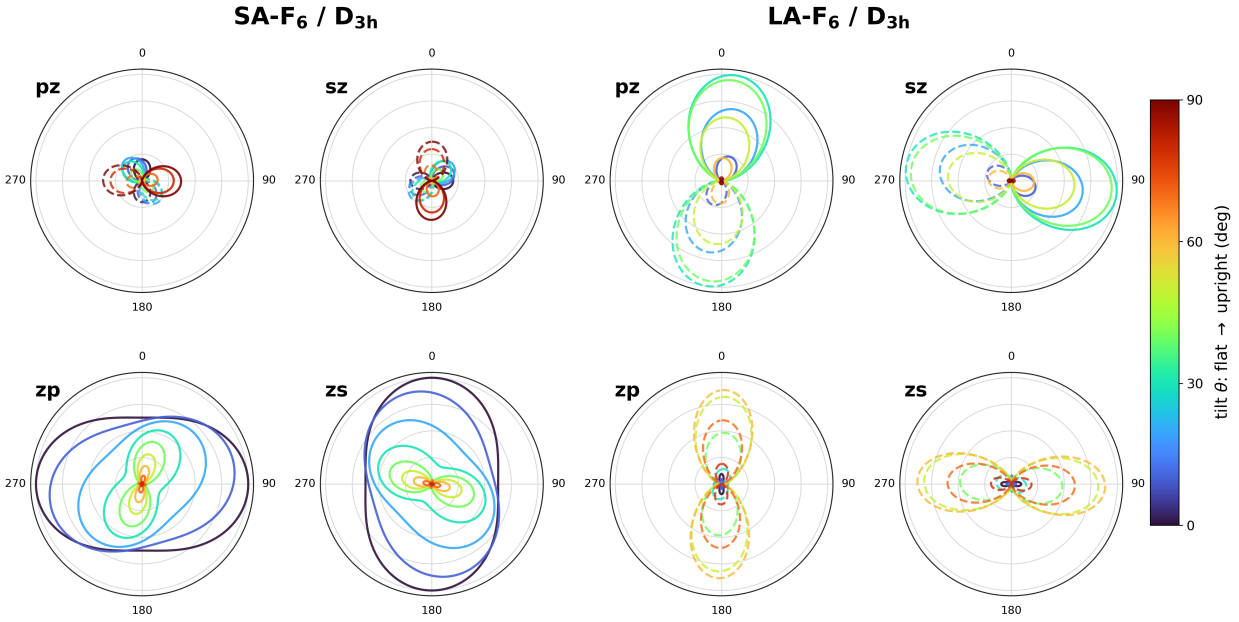

Figure S10: F_6-SA and F_6-LA mixed-z polar pattern channels on non-centrosymmetric D_{3h} monolayer-type substrate.

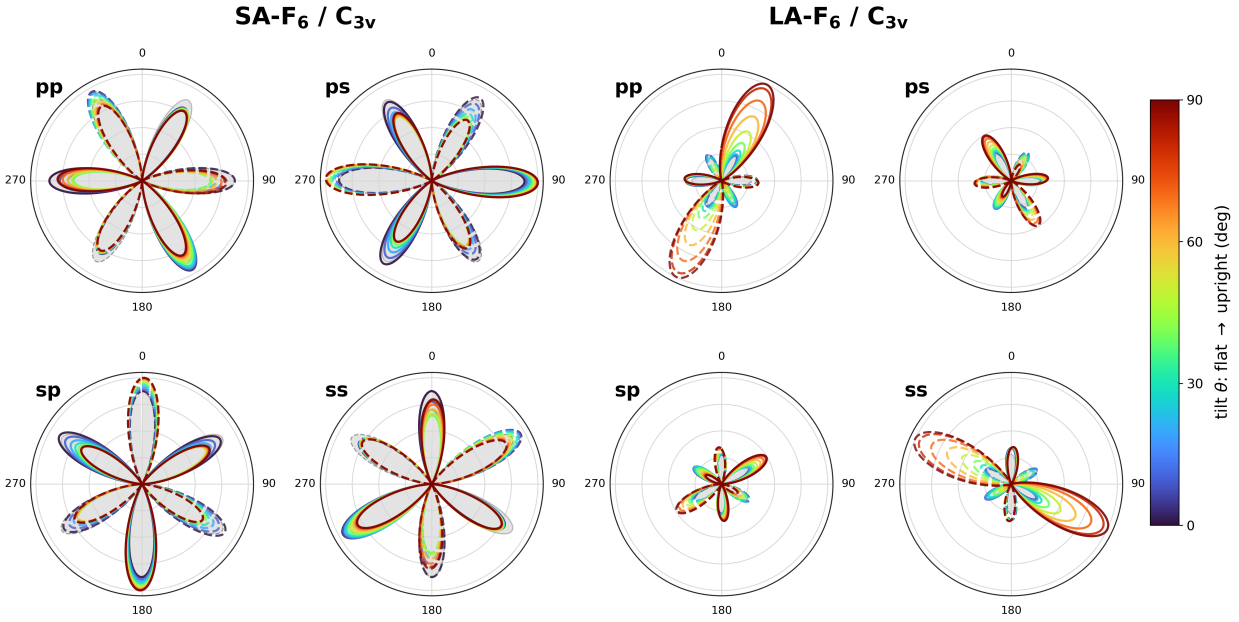

Figure S11: F_6-SA and F_6-LA in-plane polar pattern channels on the non-centrosymmetric C_{3v} Janus-type substrate. The strong in-plane response at high tilt is consistent with the channel-resolved maximum SHG as function of the tilt angle shown in the corresponding main-text channel-resolved tilt curves.

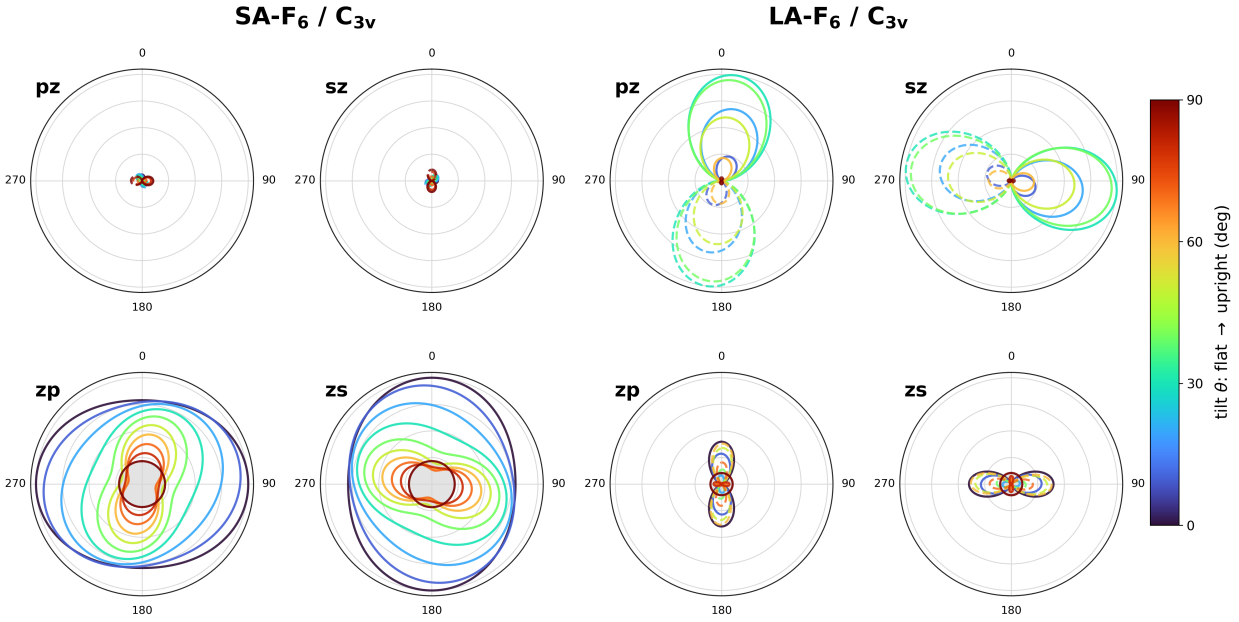

Figure S12: F_6-SA and F_6-LA mixed-z polar pattern channels on the non-centrosymmetric C_{3v} Janus-type substrate.

S3.2 Comparative Analysis with Pristine Perylene Signatures

As a control, we also evaluated pristine perylene using the same molecular SOS workflow but with the EFISH contribution omitted. This comparison is intended only to verify that the large responses discussed in the main text do not arise from the unsubstituted perylene backbone alone. The control uses one flat seed geometry; the two tilt scans shown below correspond to rigid rotations about the long molecular axis X and the short molecular axis Y. With EFISH removed, the D_{3d} response remains below 10^{-2} model units, whereas the fluorinated F_6-LA system reaches 0.084 at flat geometry and about 0.60 at near-vertical tilt. On non-centrosymmetric D_{3h} and C_{3v} substrates, pristine perylene remains close to the unit substrate background, while F_6-LA rises to approximately 3.55 at vertical tilt. This supports assigning the strongest signals to push-pull substitution, orientation-dependent molecular tensor projection, and EFISH coupling.

Table S3: Pristine-perylene control: maximum SHG intensity (model units, maximised over channel and azimuth) with EFISH excluded. The molecule has $|\mu| = 0.28$ D. Near-vertical entries are reported as X/Y, corresponding to rigid rotations about the long molecular axis X and short molecular axis Y, respectively.

Substrate symmetry	SHG ($\theta = 0°$)	SHG ($\theta = +90°$)	SHG ($\theta = -90°$)
D_{3d}	0.0064	0.0066/0.0066	0.0066/0.0066
D_{3h}	1.111	1.135/1.135	1.135/1.097
C_{3v}	1.111	1.135/1.135	1.135/1.097

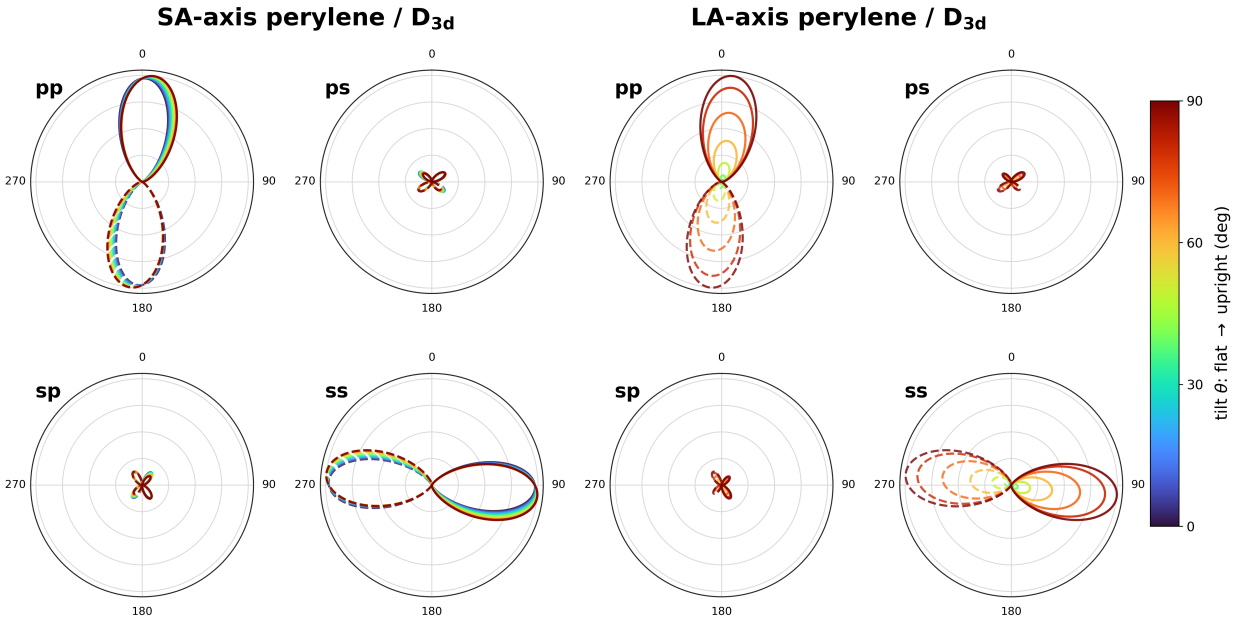

Figure S13: Continuous-tilt in-plane azimuthal SHG polar patterns for pristine perylene on the centrosymmetric D_{3d} bilayer, with EFISH excluded. The panels are shown only as a control diagnostic for two rigid rotation-axis choices of the same pristine molecule; they are not treated as distinct chemical isomers in the main-text ranking table. The SA and LA labels denote rotations about the short and long molecular axes of the perylene backbone, respectively.

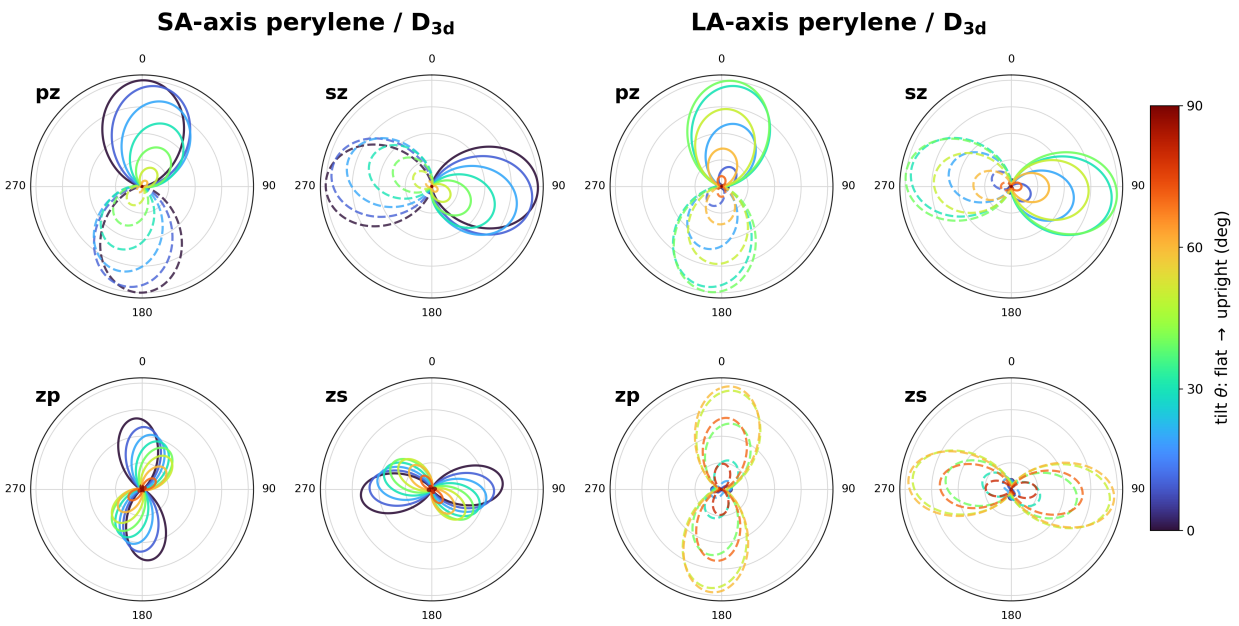

Figure S14: Continuous-tilt mixed-z azimuthal SHG polar patterns for pristine perylene on the centrosymmetric D_{3d} bilayer, with EFISH excluded. The SA and LA labels denote rotations about the short and long molecular axes of the perylene backbone, respectively.

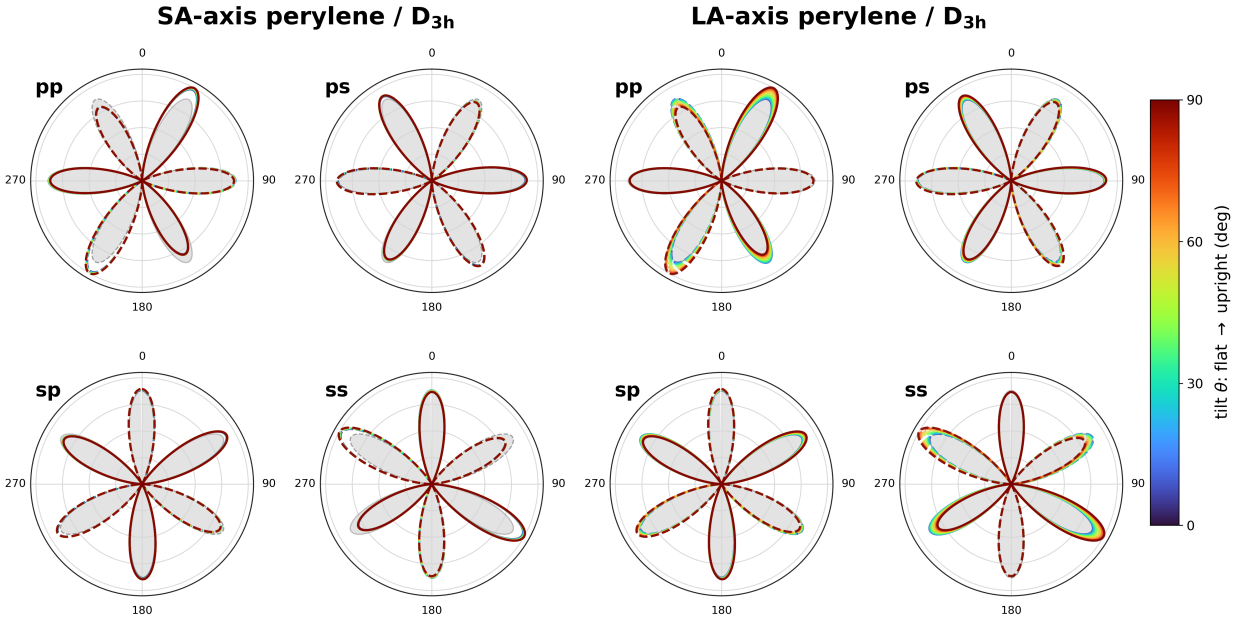

Figure S15: Continuous-tilt in-plane azimuthal SHG polar patterns for pristine perylene on the non-centrosymmetric D_{3h} monolayer substrate. The SA and LA labels denote rotations about the short and long molecular axes of the perylene backbone, respectively.

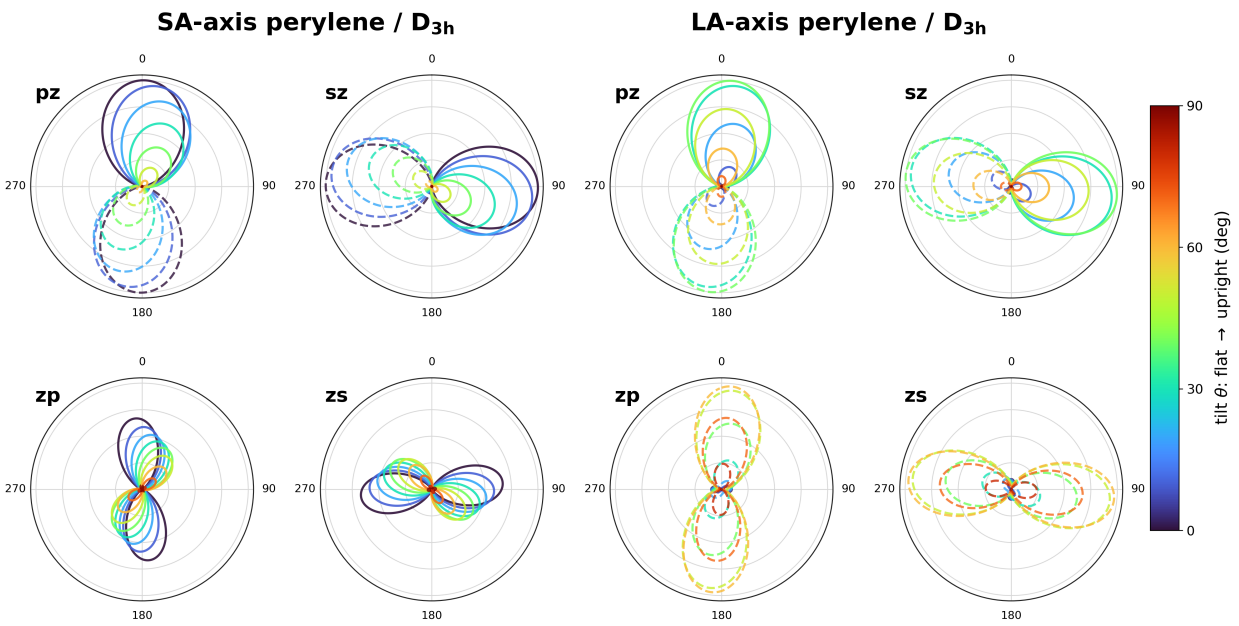

Figure S16: Continuous-tilt mixed-z azimuthal SHG polar patterns for pristine perylene on the non-centrosymmetric D_{3h} monolayer substrate. The SA and LA labels denote rotations about the short and long molecular axes of the perylene backbone, respectively.

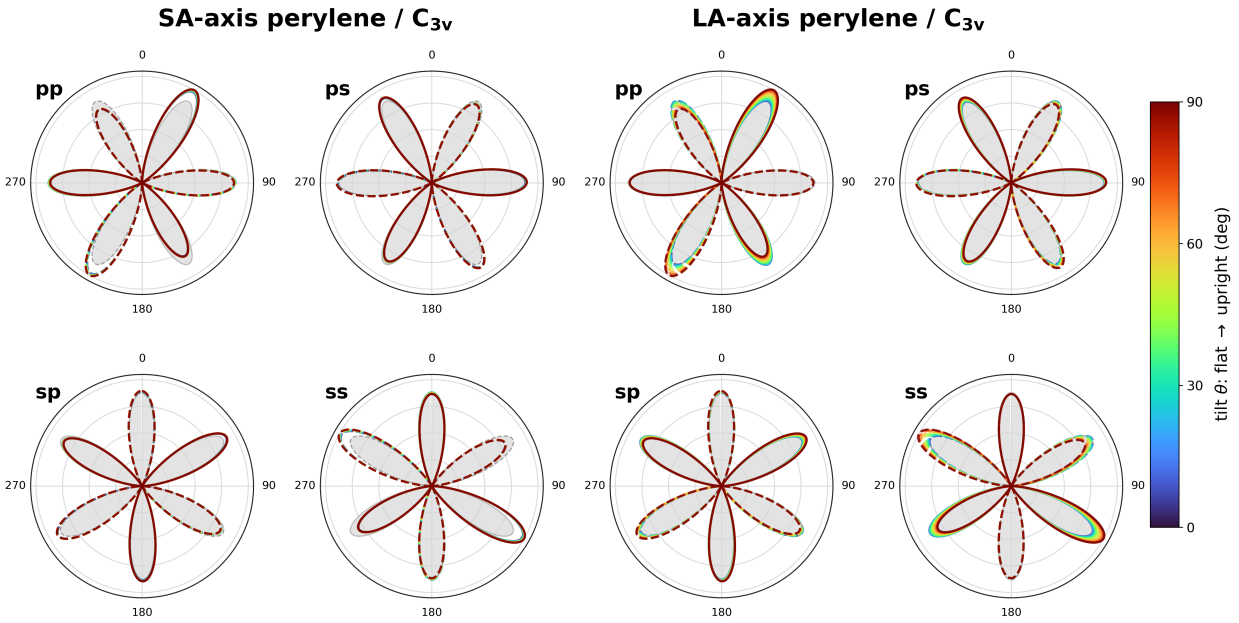

Figure S17: Continuous-tilt in-plane azimuthal SHG polar patterns for pristine perylene on the polar C_{3v} Janus-type substrate. The SA and LA labels denote rotations about the short and long molecular axes of the perylene backbone, respectively.

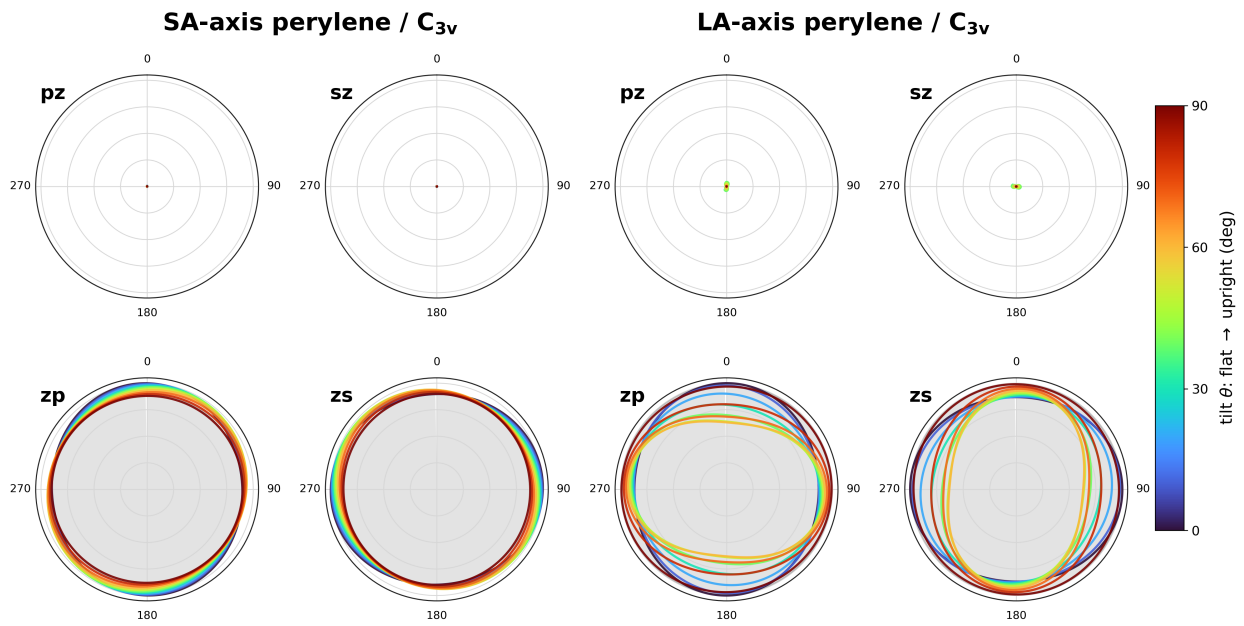

Figure S18: Continuous-tilt mixed-z azimuthal SHG polar patterns for pristine perylene on the polar C_{3v} Janus-type substrate. The SA and LA labels denote rotations about the short and long molecular axes of the perylene backbone, respectively.

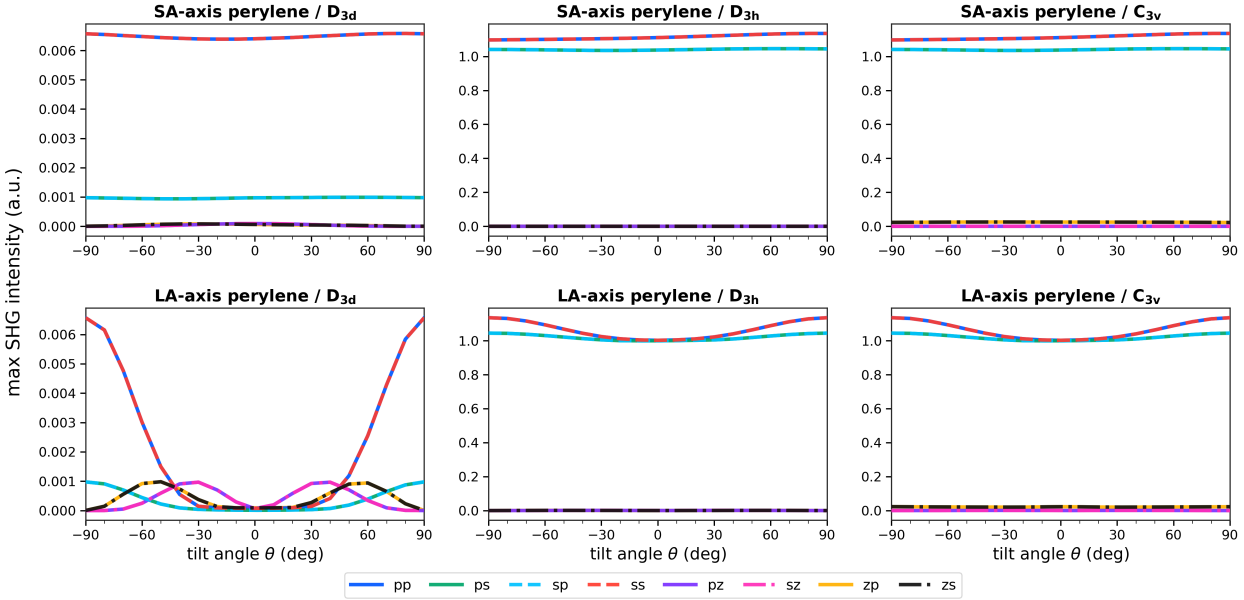

Figure S19: Channel-resolved maximum SHG intensity for pristine perylene as a function of signed tilt angle on the three model substrates. The SA and LA labels denote rotations about the short and long molecular axes of the perylene backbone, respectively.

S4 First-Principles Analysis of Selected Hybrid Organic/Inorganic Interfaces

To validate the physical assumptions behind our model framework, we performed density functional theory (DFT) calculations on a set of representative perylene/TMD hybrid interfaces, including horizontal flat-lying ($\theta = 0°$) and vertical upstanding ($\theta = 90°$). Corresponding structural models, built with the Atomic Simulation Environment (ASE) [8], included a partially fluorinated perylene molecule stacked on a 6×6 TMD supercell, resulting in a total of 140 atoms. For the host substrates, we consider representatives of the D_{3h}, D_{3d}, and C_{3v}, considering the 2H and 1T phases of MoS_2 as well as the Janus monolayers, respectively. For the Janus systems, we consider molecular adsorption on both the S-terminated (MoSeS) and the Se-terminated (MoSSe) basal planes. We examined four distinct molecular orientations: the horizontal face-to-face configuration (H) and three vertical configurations where either the hydrogenated edge ($V_{H\text{-face}}$), the fluorinated edge ($V_{F\text{-face}}$), or the mixed termination ($V_{HF\text{-face}}$) directly faces the TMD basal plane (Fig. S20).

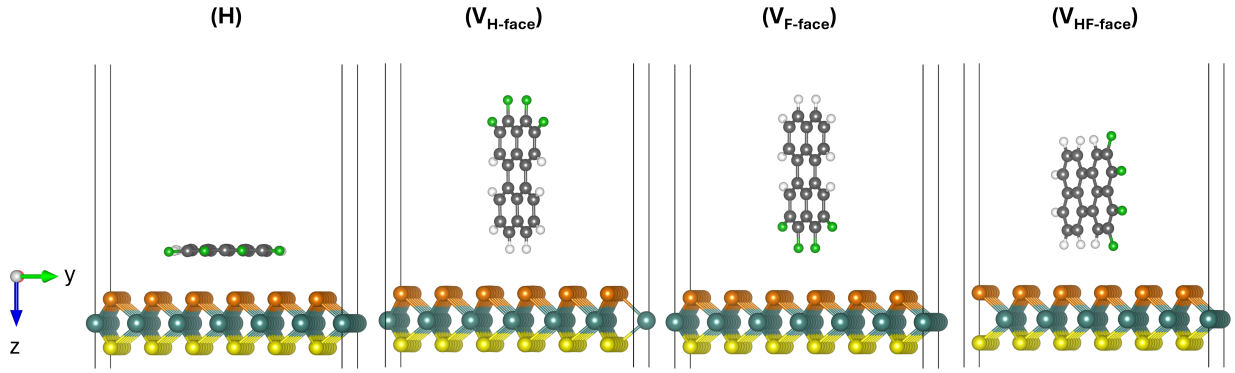

Figure S20: Schematic representations of the four considered hybrid interface geometries: the horizontally aligned configuration (H, $\theta = 0°$) and three distinct vertical orientations ($\theta = 90°$) displaying the hydrogenated edge ($V_{H\text{-face}}$), the fluorinated edge ($V_{F\text{-face}}$), and the mixed termination ($V_{HF\text{-face}}$) facing the substrate. The substrate represents a MoSSe monolayer with Mo, S, and Se atoms depicted in teal, yellow, and orange, respectively. In the molecule, C, F, and H atoms are represented by gray, green, and white spheres.

All electronic structure calculations were carried out using the Vienna ab-initio simulation Package (VASP) code [9]. Electron-nuclear interactions were described using the projector augmented wave method [10], with the Perdew-Burke-Ernzerhof (PBE) generalized gradient approximation handling the exchange-correlation potential [11]. Long-range dispersion interactions were accounted for via the semi-empirical DFT-D3 correction of Grimme equipped with the Becke–Johnson damping function [12]. A plane-wave kinetic energy cutoff of 400 eV and a Γ-centered $2 \times 2 \times 1$ **k**-point mesh were employed to sample the Brillouin zone. Total energy and residual atomic force convergence thresholds were set to 10^{-6} eV and 20 meV/Å, respectively. A vacuum spacing of 30 Å was introduced along the non-periodic surface normal to prevent unphysical interactions between periodic images. Ground-state interfacial charge transfer was quantified via the Bader charge partition scheme [13].

Across all substrates, the horizontal configuration represents the energetic global minimum for molecular adsorption (Table S4). Forcing the system into an upright orientation yields an energetic penalty between 1.02 eV and 1.26 eV, depending on the specific substrate and edge termination.

Table S4: Calculated adsorption distance (d), binding energy (E_b), and net ground-state interfacial charge transfer (Δq) for the 16 configurations. Positive values of Δq denote electron transfer from the molecule to the substrate.

Substrate	**Configuration**	d **(Å)**	E_b **(eV)**	Δq (e)
1T–MoS_2	H	3.0	-2.57	0.083
	$V_{F\text{-face}}$	3.1	-1.37	0.048
	$V_{H\text{-face}}$	2.5	-1.52	0.189
	$V_{HF\text{-face}}$	3.1	-1.51	0.148
2H–MoS_2	H	3.2	-2.62	0.013
	$V_{F\text{-face}}$	3.2	-1.40	-0.016
	$V_{H\text{-face}}$	2.5	-1.52	-0.013
	$V_{HF\text{-face}}$	2.6	-1.60	-0.024
MoSSe (Se-face)	H	3.3	-2.29	-0.026
	$V_{F\text{-face}}$	3.1	-1.04	-0.024
	$V_{H\text{-face}}$	2.5	-1.12	-0.023
	$V_{HF\text{-face}}$	2.7	-1.22	-0.035
MoSeS (S-face)	H	3.2	-2.24	0.008
	$V_{F\text{-face}}$	3.1	-0.98	-0.017
	$V_{H\text{-face}}$	2.7	-1.12	-0.013
	$V_{HF\text{-face}}$	2.6	-1.21	-0.028

Despite this clear preference for face-to-face adsorption, the large and negative binding energies preserved across all vertical configurations, falling orders of magnitude below the room-temperature thermal energy, confirm that these orientation states correspond to physically stable structural minima that can be reached under realistic deposition or kinetic growth conditions.

Moreover, on both 2H–MoS_2 and Janus substrates, the net ground-state interfacial charge transfer (Δq) remains extremely small, never exceeding 0.04 e. Even on the 1T–MoS_2 phase, charge transfer remains restricted to $\Delta q < 0.20$ e, which is well below the typical chemisorption threshold. This absence of substantial charge redistribution confirms the physisorption nature of the substrate-molecule interaction, preserving the electronic integrity of the perylene core upon deposition. These findings provide a robust, first-principles justification for our assumption of an unperturbed molecular hyperpolarizability across the entire orientation sweep. Concurrently, the subtle system-dependent variations reported here motivate future atomistic studies to fully elucidate excited-state interaction mechanisms beyond the physics captured by our model.

References

[1] B. J. Orr and J. F. Ward. Perturbation theory of the non-linear optical polarization of an isolated system. *Mol. Phys.*, 20(3):513–526, 1971. doi: 10.1080/00268977100100481.

[2] Mark E. Casida. Time-dependent density-functional theory for molecules and molecular solids. *J. Mol. Struct.: THEOCHEM*, 914(1):3–18, 2009. ISSN 0166-1280. doi: https://doi.org/10.1016/j.theochem.2009.08.018. URL https://www.sciencedirect.com/science/article/pii/S0166128009005363. Time-dependent density-functional theory for molecules and molecular solids.

[3] N. Tancogne-Dejean, M. J. T. Oliveira, X. Andrade, et al. Octopus, a computational framework for exploring light-driven phenomena and quantum dynamics in extended and finite systems. *J. Chem. Phys.*, 152:124119, 2020.

[4] C. Hartwigsen, S. Goedecker, and J. Hutter. Relativistic separable dual-space gaussian pseudopotentials from h to rn. *Phys. Rev. B*, 58:3641–3662, Aug 1998. doi: 10.1103/PhysRevB.58.3641. URL https://link.aps.org/doi/10.1103/PhysRevB.58.3641.

[5] J. P. Perdew and Alex Zunger. Self-interaction correction to density-functional approximations for many-electron systems. *Phys. Rev. B*, 23:5048–5079, May 1981. doi: 10.1103/PhysRevB.23.5048. URL https://link.aps.org/doi/10.1103/PhysRevB.23.5048.

[6] J. Krumland, G. Gil, S. Corni, and C. Cocchi. LayerPCM: An implicit scheme for dielectric screening from layered substrates. *J. Chem. Phys.*, 154:224114, 2021.

[7] H. Autere, H. Jussila, Y. Dai, Y. Wang, H. Lipsanen, and Z. Sun. Nonlinear optics with 2d layered materials. *Adv. Mater.*, 30:1705963, 2018.

[8] Ask Hjorth Larsen, Jens Jørgen Mortensen, Jakob Blomqvist, Ivano E Castelli, Rune Christensen, Marcin Dułak, Jesper Friis, Michael N Groves, Bjørk Hammer, Cory Hargus, et al. The atomic simulation environment—a python library for working with atoms. *J. Phys. Condens. Matter.*, 29(27):273002, 2017.

[9] G. Kresse and J. Furthmüller. Efficient iterative schemes for ab initio total-energy calculations using a plane-wave basis set. *Phys. Rev. B*, 54:11169–11186, Oct 1996. doi: 10.1103/PhysRevB.54.11169. URL https://link.aps.org/doi/10.1103/PhysRevB.54.11169.

[10] P. E. Blöchl. Projector augmented-wave method. *Phys. Rev. B*, 50:17953–17979, Dec 1994. doi: 10.1103/PhysRevB.50.17953. URL https://link.aps.org/doi/10.1103/PhysRevB.50.17953.

[11] John P. Perdew, Kieron Burke, and Matthias Ernzerhof. Generalized gradient approximation made simple. *Phys. Rev. Lett.*, 77:3865–3868, Oct 1996. doi: 10.1103/PhysRevLett.77.3865. URL https://link.aps.org/doi/10.1103/PhysRevLett.77.3865.

[12] Stefan Grimme, Stephan Ehrlich, and Lars Goerigk. Effect of the damping function in dispersion corrected density functional theory. *J. Comput. Chem.*, 32(7):1456–1465, 2011.

[13] Graeme Henkelman, Andri Arnaldsson, and Hannes Jónsson. A fast and robust algorithm for bader decomposition of charge density. *Comp. Mater. Sci.*, 36(3):354–360, 2006.